ACS Photonics

pubs.acs.org/journal/apchd5

Article

Engineering and Microscopic Mechanism of Quantum Emitters Induced by Heavy Ions in hBN

Rui Gu, Lei Wang, Huiping Zhu, Shuangping Han, Yurong Bai, Xuewen Zhang, Bo Li,* Chengbing Qin,* Jie Liu, Gang Guo, Xiaoting Shan, Guodong Xiong, Jiantou Gao, Chaohui He, Zhengsheng Han,* Xinyu Liu, and Fazhan Zhao

Cite This: ACS Photonics 2021, 8, 2912−2922

Read Online

ACCESS | Metrics & More | Article Recommendations | Supporting Information

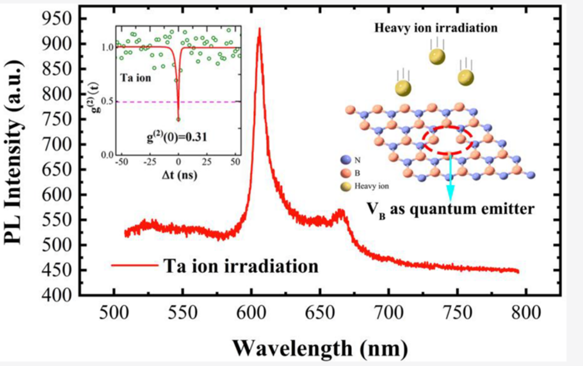

ABSTRACT: Solid-state quantum emitters play a critical role in the application of quantum information technology. Quantum emitters with high brightness at room temperature can be realized in hBN, and it has become a current research hotspot. However, much of the research up to now only produced quantum emitters at the edges and wrinkles of hBN, which tremendously limited the usage of the quantum emitters. In this work, heavy ions irradiation methods were employed to produce high-quality quantum emitters in the middle region of the hBN sample. The quantum emitter production engineering via heavy ions irradiation was systematically investigated. The dependence of irradiated ion type, energy, and fluence, as well as the thickness of the hBN flakes, on the production efficiency of the hBN quantum emitters were analyzed in detail. The characteristics of luminescence of quantum emitters, such as second-order correlation function $g^{(2)}(\tau)$, stability, polarization, and saturation, were all compared with different irradiation conditions. In addition, based on the wavelength statistical results of quantum emitters in hBN, the transition energies of various intrinsic point defects in hBN were studied through first-principles calculations to reveal the originations of luminescence. The calculation results indicated that the V_N, V_B, and B_i point defects were possible candidates of the quantum emitter centers. Overall, in this study, according to experimental characterizations, heavy ion irradiation should be an efficient method to produce stable, ultrabright, highly linearly polarized quantum emitters in hBN flakes.

KEYWORDS: *heavy ion irradiation, hBN, quantum emitters, PL mapping, production efficiency, point defects*

The application of high-quality solid-state single-photon sources in quantum communication and quantum information fields is extremely important.[1,2] Some methods have been developed to realize quantum emission in solid materials, including GaAs-based quantum dots, carbon nanotubes, point defects in Diamond, and SiC.[3−8] In recent years, the boosted two-dimensional (2D) materials have attracted major attention across multiple fields of nanoscale science and technology.[9] Some literature reported that quantum emitters could be realized in 2D WSe_2, which has high extraction efficiency and is easy to be integrated into photoelectronic devices, but it can only be operated at low temperatures.[10−13] To overcome the operation temperature, the generation of quantum emitters in hexagonal boron nitride (hBN) is attractive because of its chemical and thermal stability, especially its high brightness at room temperature.[14] The band gap of hBN is about 6 eV, and the reported zero-phonon lines (ZPLs) of quantum emitters in hBN at room temperature have a broad range that can span from near-infrared to the visible spectrum range (about 1.6−2.2 eV), even to the ultraviolet range (about 4.1 eV).[14−16]

To take advantage of 2D materials of easy integration with cavities and photonic waveguides, activation methods of quantum emitters deserve to be developed.[17−21] Recent studies have proved that quantum emitters can be generated by chemical etching, ion implantation, focused laser irradiation, argon plasma etching, focused ion beam, and other methods in 2D hBN.[9,22−24] However, quantum emitters created by these methods were mainly located at the edge or wrinkle of 2D hBN flakes,[9] which greatly limited the applications of quantum emitters. To solve this problem, some literature reported that quantum emitters could be generated in the middle region of hBN flakes by using high-energy electron beam irradiation and fast neutron irradiation.[25,26] The irradiated electrons and

Received: March 10, 2021
Published: September 8, 2021

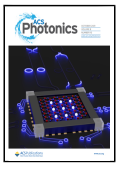

neutrons could effectively transfer a large part of the kinetic energies to B or N atoms and directly form atomic displacements,[26−28] which can produce point defects related to quantum emitters in the middle region of hBN flakes rather than just depending on intrinsic defects or dangling bonds at flake edges and grain boundaries in hBN.[26] Radiation damage can be divided into ionizing radiation damage and nonionizing radiation damage. Ionizing radiation damage means that incident ions generate a large number of electron−hole pairs in the semiconductor, which seriously affects its electrical properties. Nonionizing radiation damage refers to the collision of incident ions with lattice atoms, resulting in defects in the material.[29] However, due to the low nonionizing radiation damage of high-energy electrons and neutrons, the production efficiency and the quality of quantum emitters in hBN, such as luminescence purity, become the main factors to restrict the application of these quantum emitters.

To the best of our knowledge, high-energy heavy ions have larger nonionizing radiation damage ability than light particles, which should be better candidates to generate quantum emitters in hBN samples by irradiation. Therefore, in this work, high-energy Ta or Ge heavy ions were employed to create quantum emitters in hBN. The best engineering conditions and parameters for generating quantum emitters in hBN, such as the radiation fluence, the thickness of hBN flake, the producing position, the wavelength distribution, and quality of quantum emitter, were systematic investigated and compared. Moreover, the first-principles calculation was used to explore the microscopic origination of the quantum emitters in hBN induced by the heavy ion irradiation method.

EXPERIMENTAL SECTION

The hBN bulk material was made by the chemical vapor deposition method. The layered hBN samples were first exfoliated from bulk hBN by mechanical exfoliation method, and then transferred onto Si/SiO_2 substrates with an area of 1 $\times$ 1 cm^2. The optical image of a typical hBN flake on Si/SiO_2 is shown in Figure 1a. These hBN samples were annealed in a

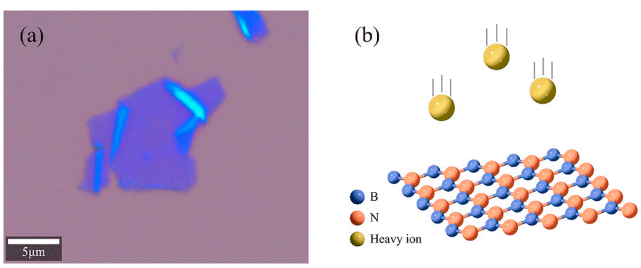

Figure 1. (a) Optical image of the typical hBN flake. (b) Schematic diagram of 2D-hBN with Ta or Ge ions irradiation.

furnace with 1 Torr argon atmosphere for stability. The annealing temperature of hBN increased from 20 to 850 °C in 60 min, maintaining about 60 min, and then reduced to 20 °C during 480 min. The heavy ion irradiation experiments were realized in an ion accelerator with a vacuum chamber at room temperature. Half of the hBN samples were irradiated by a Ta ion with an energy of 1907 MeV, and the other samples were irradiated by a Ge ion with an energy of 208 MeV. The fluences of the Ta ion were set to be 5×10^7, 1×10^8, and 1×10^9 ions/cm^2, and the fluences of the Ge ion were set to be 1×10^8, 1×10^9, and 1×10^{10} ions/cm^2, respectively. Both Ta and Ge ion beams were sent vertically to hBN samples. The schematic diagram of the high-energy ion irradiation experiment is shown in Figure 1b.

Based on SRIM software simulation, the penetration depths of Ta ions and Ge ions in hBN are 98 and 26 μm, respectively. Ta or Ge ions had enough energy to penetrate the whole hBN flakes so that no doping effect was considered in this study. The thickness of hBN flakes was measured by an atomic force microscope (AFM). Photoluminescence (PL) mapping was carried out by a WITec confocal Raman fluorescence spectrometer to search the position of quantum emitters and characterize their properties in irradiated 2D hBN samples. The excitation wavelength was chosen as 473 nm, which could realize PL and Raman characterization in the visible light spectrum range. The excitation polarization of the quantum emitter was controlled using a half-wave plate, which was placed in the incident light path. Moreover, a laser power meter was installed in the incident light path to characterize the change of PL with excitation power (characterizing the fluorescence saturation behavior). To prove the quantum characteristics of the defect's luminescence, a Hanbury Brown and Twiss (HBT) interferometer was used to record the second-order correlation function $g^{(2)}(\tau)$ of PL. In particular, the collected PL was split by a 50:50 beam splitter and then detected by two single-photon detectors through time-correlated single-photon counting (TCSPC) technique. $g^{(2)}(\tau)$ can be determined by calculating the coincidences at different time delays (τ) between two detectors. For an ideal N-photon source, $g^{(2)}(0) = 1 - 1/N$. Thus, the condition, $g^{(2)}(0) < 0.5$, is generally defined as the criterion of a quantum emitter (a single-photon source).

Before heavy ion irradiation, original hBN thin films were annealed and characterized by PL mapping. No significant PL intensities can be determined, indicating the high crystalline quality of the original hBN. Therefore, all the quantum emitters observed in this study should be produced by heavy ion irradiation.

RESULTS AND DISCUSSION

Figure 2 shows the typical PL spectra of quantum emitters in 2D hBN samples induced by high-energy Ta and Ge ions irradiation. Figure 2a−c corresponds to the Ta ion fluences of 5×10^7, 1×10^8, and 1×10^9 ions/cm^2, while Figure 2d−f corresponds to the Ge ion fluences of 1×10^8, 1×10^9, and 1×10^{10} ions/cm^2, respectively. The inset in each figure is the image of PL-mapping of hBN flakes, and the green circle represents the location of the PL spectrum. The typical PL spectra induced by heavy ions are almost the same as previously reported in the literature.[14,30−34] Most spectra show a clear ZPL and a broad shoulder peak, which is called phonon sideband (PSB). ZPL is defined as the direct transition energy between energy bands when no phonons are involved. On the contrary, PSB refers to the participation of phonons in the transition process. Based on the statistics of the energy gap between ZPL and PSB, the results indicate that the energy interval are mostly around 163 and 186 meV (see Supporting Information, S1), which may be consistent with the energy of transverse optical phonons and longitudinal optical phonons, respectively.[35−39] In addition, for both Ta and Ge ions irradiation, it is interesting to note in Figure 2 that the background noise of the PL spectrum becomes larger as irradiation ion fluence increases.

https://doi.org/10.1021/acsphotonics.1c00364
ACS Photonics 2021, 8, 2912−2922

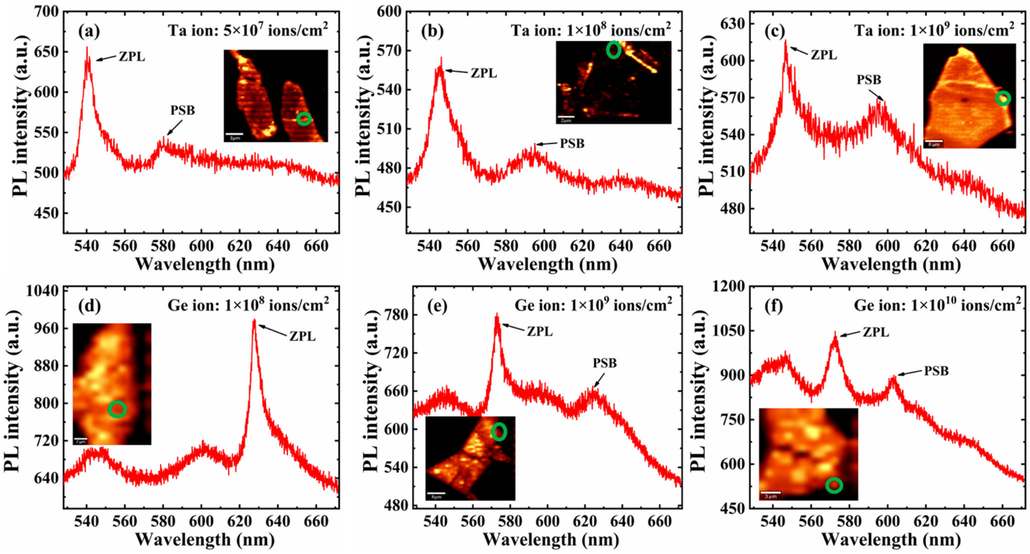

Figure 2. Typical PL spectrum of quantum emitters extracted from samples irradiated by Ta and Ge ions, and ion fluences are marked in each figure. The inset is the PL-mapping scan result of the 2D hBN flake, and the green circle represents the position of the quantum emitters. For the PL-mapping scan, the experimental test was performed at room temperature with 473 nm continuous wave excitation. All spectra were collected at a laser pumping power of 7 mW and an integration time of 1 s.

To obtain the best engineering conditions via the heavy ion irradiation method, the numbers of quantum emitters in hBN flakes generated by heavy ions are statistically analyzed. The influence of heavy-ion type, irradiated ion fluence, and the thickness of hBN films on the production efficiency and production position of the quantum emitters is studied in detail.

Table 1 shows the number of quantum emitters produced under different Ta and Ge ion fluences and the scanning area of PL-mapping. In this study, the production efficiency of quantum emitters is defined as the number of quantum emitters generated in hBN flakes divided by the area of PL mapping. From Table 1, based on the ion fluence splits, it is clear to see that both Ta and Ge ion irradiations follow similar variation trends of production efficiency, that is, the production efficiency first increases with ion fluence and reaches a maximum value, then decreases with further ion fluence increases. The maximum production efficiency of 0.0213 counts/μm^2 can be obtained when hBN exposed to Ta ions with a fluence of 1×10^8 ions/cm^2, which is much larger than 0.0117 counts/μm^2 with the optimal irradiation fluence of Ge ions of 1×10^8 ions/cm^2. This phenomenon indicates that the higher energy of irradiated ions is beneficial to quantum emitter production.

Table 1. Statistical Number and Production Efficiency of Quantum Emitters in 2D hBN under Different Irradiated Ion Types and Fluences

	fluence (ions/cm^2)	No. of quantum emitters (counts)	area of PL mapping (μm^2)	production efficiency (counts/μm^2)
Ta ion	5×10^7	13	2374	0.0055
	1×10^8	32	1499	0.0213
	1×10^9	20	4224	0.0047
Ge ion	1×10^8	9	1220	0.0074
	1×10^9	21	1788	0.0117
	1×10^{10}	9	1635	0.0055

The nonmonotonic variation of production efficiency with ion irradiation fluence in Table 1 can be explained by the irradiation-induced atom displacement damage effect. For Ta ions, when the ion fluence was 5×10^7 ions/cm^2, the crystalline defects started to come out in hBN, but atom displacement damage of Ta was insufficient, thus the number of point defects related to quantum emitters increased as ion fluence increasing. When ion fluence reached 1×10^8 ions/cm^2, the production efficiency rose to its maximum value (based on the three ion fluence splits in this study). For the Ta ion fluence of 1×10^9 ions/cm^2, too many defects were generated, resulting in a short distance between the point defects, which seriously affects the quantum performance of the quantum emitter, as reported in the literature.[40] Moreover, it may form a very large defect structure, so that defect luminescence becomes classic luminescence. As a result, the production efficiency sharply decreased under high fluence. Because the atom displacement damage capacity of Ge ion is weaker than Ta ions, the production efficiency of quantum emitters by Ge ion irradiation at the same fluence is lower than that by Ta ions. This conclusion is consistent with the results reported in the literature,[41] which pointed out that the existence of luminescence point defects at low enough density can enable a few quantum emitters to be isolated and be stable at room temperature.

Besides irradiated ion type, energy, and fluence, the thickness of 2D hBN flake is another critical parameter to the production efficiency of quantum emitters. Based on the PL mapping analysis, the influences of 2D hBN flake thickness on the production efficiency of quantum emitters were also analyzed and compared. Figure 3 shows the images of the hBN flakes that are most likely to generate quantum emitters under the different fluence of Ta and Ge ions. The accurate thickness of each hBN flake was measured by AFM, and these thicknesses are also marked in Figure 3. The statistical results indicate that for Ta ion with a fluence of 5×10^7 ions/cm^2, the 4 nm thick hBN flake has the highest production efficiency of quantum emitters. For Ta ions with the fluence of 1×10^8

https://doi.org/10.1021/acsphotonics.1c00364
ACS Photonics 2021, 8, 2912−2922

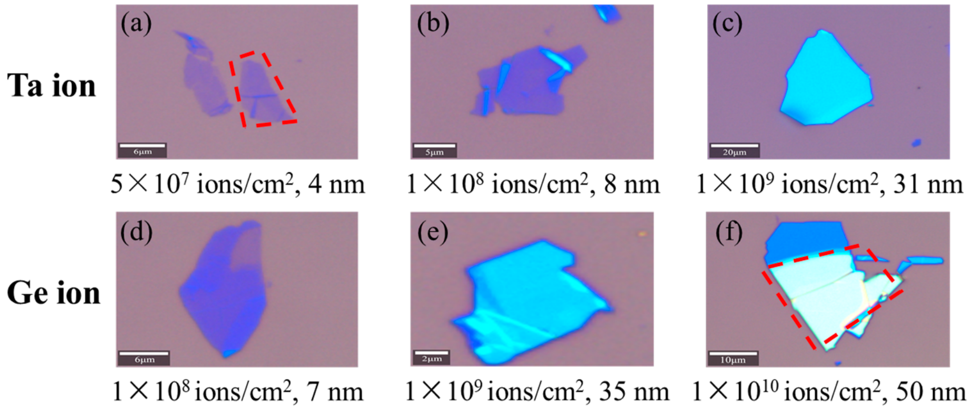

Figure 3. Optical image of hBN flakes with the best production efficiency under different ion types and ion fluences. (a), (b), and (c) are the images of hBN flakes under Ta ion irradiation with the fluences of 5×10^7, 1×10^8, and 1×10^9 ions/cm^2. (d), (e), and (f) are the images of hBN flakes with Ge ions irradiation under the fluences of 1×10^8, 1×10^9, and 1×10^{10} ions/cm^2. The areas marked by the red dotted line are the measured areas in some slices. The irradiation fluence and thickness of each hBN flake are marked below the picture.

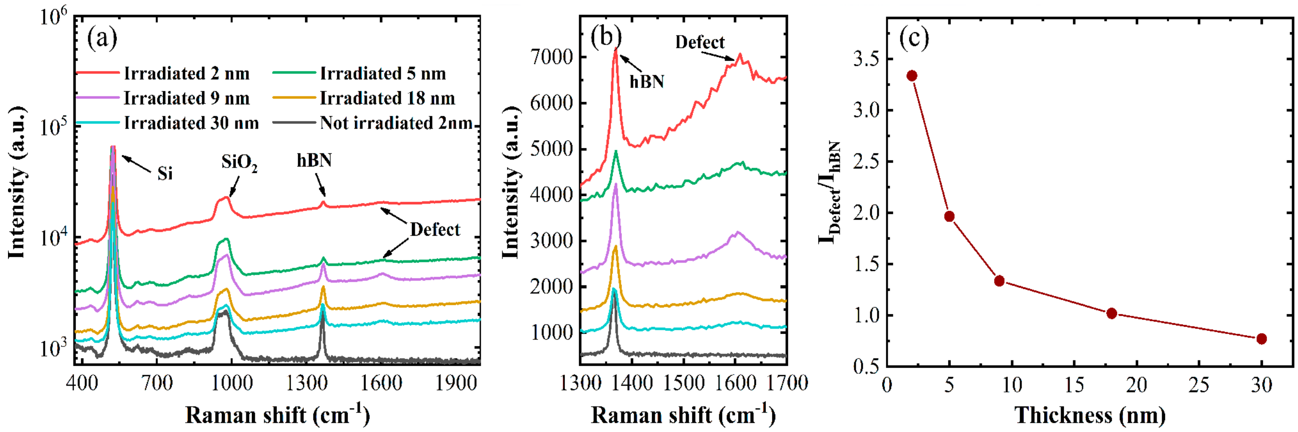

Figure 4. (a) Raman spectra of the original 2 nm hBN and irradiated hBN flakes with different typical thicknesses. The irradiation fluence was chosen to be 1×10^9 ions/cm^2. All spectra were collected at a pumping laser power of 9 mW and integrated 10 s. (b) Partially magnified hBN Raman peak and defect peak in (a). (c) The integrated intensity ratio of the defect peak to intrinsic peak as a function of the hBN thickness after irradiation.

ions/cm^2, optimal thickness for the highest production efficiency increases to 8 nm, while for ion fluence of 1×10^9 ions/cm^2, the thickness continuously increases to 31 nm. The trend of Ge ion is similar to Ta ion. In detail, 7, 35, and 50 nm are the best thicknesses for production efficiency of quantum emitters under the Ge ion fluence of 1×10^8, 1×10^9, and 1×10^{10} ions/cm^2, respectively. This analysis reveals that the optimal thickness of 2D hBN for production efficiency of quantum emitters increases with the fluences of both Ta and Ge ions.

It is reported in the literature that the damage threshold of graphene under irradiation increased with the number of layers.[42] Therefore, we speculate that the interaction between layers in 2D hBN flake plays a crucial role to influence the point defect generation due to heavy ion irradiation. To further investigate the relationship between production efficiency of quantum emitters and layer thickness, in general, the integrated intensity ratio of defect peak to intrinsic peak in graphene Raman spectrum is mainly used to characterize the damage intensity of graphene samples under irradiation.[42,43] Since hBN is a graphene-like structure, this method should be also applicable to characterize the hBN samples.

Raman characterization was performed on the original hBN flake (2 nm) and irradiated hBN flakes with different typical thicknesses (2, 5, 9, 18, and 30 nm). hBN flakes under Ta ion irradiation with a fluence of 1×10^9 ions/cm^2 were selected in Raman measurements. The Raman spectra are shown in Figure 4a. The intrinsic Raman peak of Si at 520 cm^{-1}, SiO_2 related Raman peak at 970 cm^{-1}, and intrinsic Raman peak of hBN at 1369 cm^{-1} are all clearly shown.[44−46] It is clear to see that additional Raman peaks at 1609 cm^{-1} (marked as Defect) appear in hBN flakes after exposure to Ta ion irradiation with a fluence of 1×10^9 ions/cm^2. Therefore, the Raman peak at 1609 cm^{-1} in this study can be attributed to a defect-related peak caused by irradiation. To further observe and study the relationship between the defect peak and the thickness of the hBN flakes more clearly, a partial enlargement of the defect peak and hBN peak is shown in Figure 4b. The integrated intensity ratio of the hBN defect Raman peak to hBN intrinsic Raman peak was calculated to characterize the strength of hBN samples damaged, and the relationship between the ratio value and the thickness of hBN is shown in Figure 4c. The experimental results indicate that the thinner hBN flakes are more susceptible to damage, and the atom displacement damage effect induced by irradiation becomes weakened as the hBN thickness increases. Most of the hBN flakes appear to have similar trends, but there are also some exceptions in this study (more detailed statistics in Supporting Information, S2).

https://doi.org/10.1021/acsphotonics.1c00364
ACS Photonics 2021, 8, 2912−2922

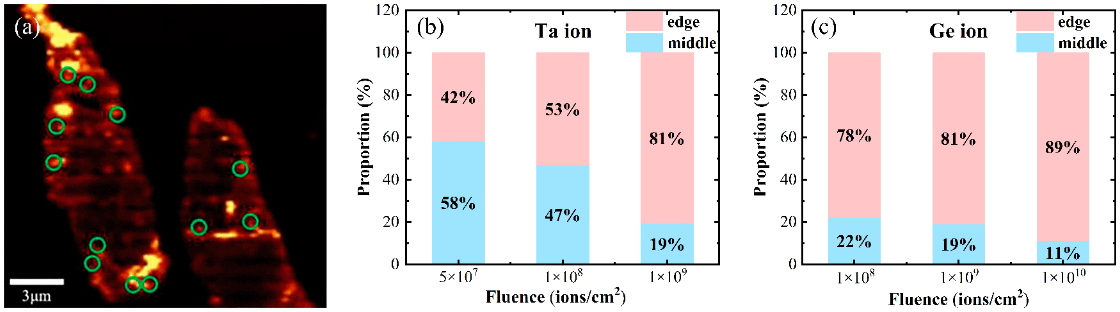

Figure 5. (a) Typical image of location of quantum emitters in hBN, and the green circles represent the locations of quantum emitters. 2D hBN thickness: 4 nm; irradiation condition: Ta ions, 5×10^7 ions/cm^2. (b) and (c) are the proportion of quantum emitters generated at the different region of 2D hBN flakes irradiated by Ta and Ge ions, respectively. The pink and light blue histograms represent the quantum emitters at the edge and middle of hBN flakes, respectively.

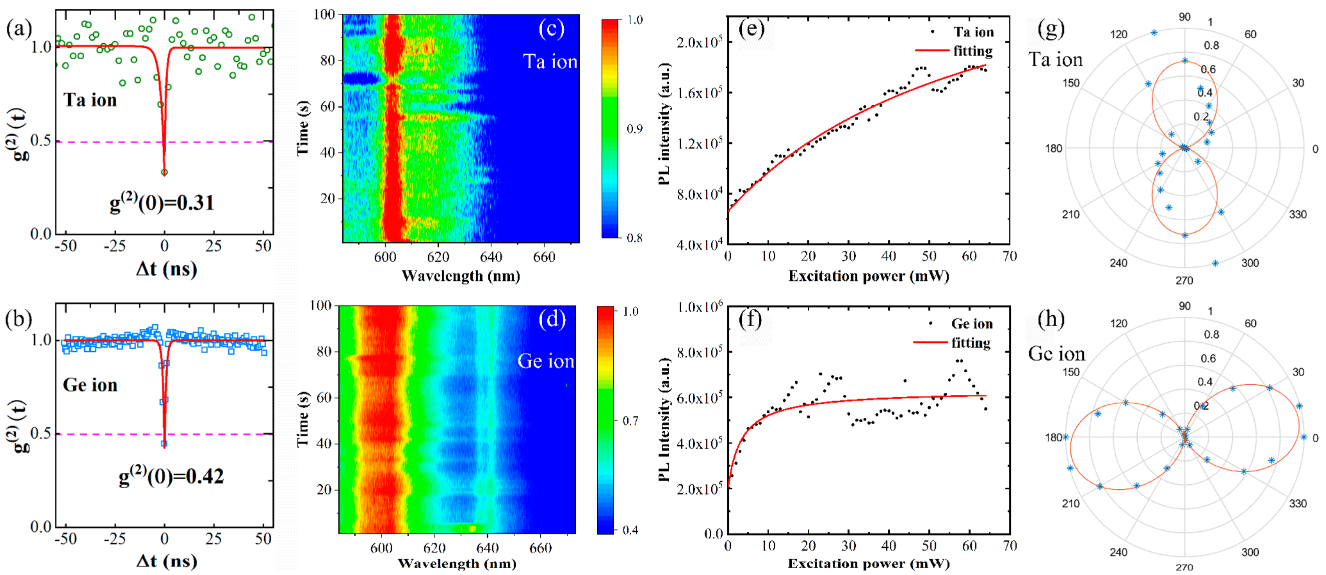

Figure 6. (a), (c), (e), and (g) are the experimental characterizations of a quantum emitter with a peak wavelength of 604 nm induced by Ta ions with fluence of 1×10^8 ions/cm^2. (b), (d), (f), and (h) are the experimental characterization of the quantum emitter (peak wavelength is 600 nm) induced by Ge ions with fluence of 1×10^9 ions/cm^2. (a) and (b) are the second-order correlation functions of the quantum emitters. The excitation wavelength of the selected laser is 532 nm. (c) and (d) are the time traces of the PL spectra of quantum emitters. The excitation power is 7 mW and integration time is 1 s. (e) and (f) are the fluorescence saturation curves and corresponding theoretical fits of quantum emitters. The saturation of PL was performed at room temperature with 473 nm continuous wave laser excitation. The excitation power is 7 mW. (g) and (h) are the PL polarization properties of quantum emitters. The polarization of PL was performed at room temperature with 473 nm continuous wave laser excitation. The excitation power is 7 mW and the integration time is 3 s. Solid red lines are fitting curves by a $\cos^2(\theta)$ function to obtain the degree of polarization, and the integration time is 1 s.

Some literature reported that both the interlayer binding energy and the exfoliation energy could be enhanced as the number of layers of 2D material increased, since the interaction force between layers became larger with the number of layers increasing.[47,48] According to the theory above and the Raman data analysis, the relationship between the optimal thickness of hBN for the quantum emitter and irradiated ion fluence could be explained as follows. Certain ion fluence has a corresponding optimal hBN thickness. Below the optimal thickness, due to the less interaction between layers in the 2D hBN flake, the atom displacement damages are too severe, and isolated fluorescent point defects are destroyed, resulting in a reduction in the production efficiency of quantum emitters. Above the optimal thickness, the atom displacement damage effect is suppressed due to the enhancement of the interaction between layers in the 2D hBN flake, such as interlayer binding energy and exfoliation energy. Only for the hBN with optimal thickness, there is a balance between the displacement damage and the layer interaction, and the number of point defects associated with the quantum emitters can reach its maximum. This is the reason for the existent of an optimal thickness for quantum emitters under certain ion fluence and the increase of optimal thickness as ion fluence increasing.

Electrical pumped quantum emitters operating at room temperature are necessary for actual applications. However, most quantum emitters in 2D hBN created by other methods located at the edge or wrinkle of hBN flakes,[9] which greatly limited the heterogeneous integration to realize electrical pumping. In this study, heavy ions can transfer their energy and momentum to B or N atoms in hBN through the atomic displacement effect, which can effectively generate point defects in the middle region of hBN flakes. Therefore, the location of quantum emitters in hBN flakes induced by Ta and Ge ions irradiation is investigated.

Figure 5a shows the location of quantum emitters in 4 nm hBN exposed to Ta ions irradiation with a fluence of 5×10^7

ions/cm^2. The green circles represent the locations of quantum emitters. It is clear to see that many quantum emitters locate in the middle of the 2D hBN, proving that heavy ion irradiation is a good method to create quantum emitters for heterogeneous integration. Based on the statistical analysis, it is interesting to note that the ion fluence can also affect the generation position of the quantum emitters. Figure 5b,c shows the proportion of quantum emitters appearing in the middle and edge regions of the hBN irradiated by Ta and Ge ions, respectively. The green histogram represents the section of quantum emitters in the middle region, while the blue histogram represents the ones in the edge region. For Ta ions, under the fluence of 5×10^7 ions/cm^2, more than half of quantum emitters (58%) are generated in the middle region of hBN flakes. When ion fluence reaches 1×10^8 ions/cm^2, the proportion of the middle region decreases to 47%, then under the fluence of 1×10^9 ions/cm^2, more than 80% of quantum emitters are generated at the edge of hBN flakes. For Ge ions, the variation of the proportion of quantum emitters in the middle region of hBN as a function of ion fluence is similar to Ta ions. However, it can be concluded from Figure 5 (b) and (c) that, compared with Ge ions, Ta ions can generate more quantum emitters in the middle region of hBN flakes, which is probably attributed to the lower damage ability of Ge ions than that of Ta ions. Overall, proper irradiated ion type, energy, and fluence can create an appreciable quantity of quantum emitters in the middle of hBN flakes, which is a significant advantage of the heavy ion irradiation method.

After completing the statistical analysis of quantum emitters, it is necessary to characterize the luminescence quality of the quantum emitters generated by the heavy ion irradiation method. First, it is necessary to prove that the point defects generated by heavy ions in hBN are quantum emitters. To demonstrate that the point defects produced by heavy-ion irradiation are quantum emitters, we recorded second-order correlation functions $g^{(2)}(\tau)$ of defects. In addition, an ideal quantum emitter should satisfy high luminescence stability, a high degree of linear polarization, and large fluorescence intensity.[41] In this study, the quantum emitters in 2D hBN with the peak wavelength of 600 nm induced by Ta and Ge ions were selected for measuring $g^{(2)}(\tau)$, stability, saturation, and polarization analysis to characterize the quality of these quantum emitters.

From Figure 6a, we can determine the dip of PL coincidences, generated by Ta ions in hBN, at zero-delay is well below 0.5 ($g^{(2)}(0) = 0.31$), indicating that it is a quantum emitter or a single-photon source. Figure 6b shows the second-order correlation function of the point defect generated by Ge ions in hBN, where the dip at zero-delay is also well below 0.5 ($g^{(2)}(0) = 0.42$), indicating that it is also a quantum emitter. We have confirmed that the low values of $g^{(2)}(0)$ can be well reproduced on other emitters. The second-order correlation value of the quantum emitters produced by Ta ions in hBN is lower than that of the quantum emitters produced by Ge ions, which indicates that the quantum emitters produced by Ta ions have superior quantum performance.

Figure 6c shows the PL spectrum stability of a quantum emitter with a peak wavelength of 604 nm, produced by Ta ions under the fluences of 1×10^8 ions/cm^2, and Figure 6d shows the PL spectrum stability of a quantum emitter with a peak wavelength of 600 nm, produced by Ge ions under the ions fluences of 1×10^9 ions/cm^2. The sustaining time was set to be 100 s. It can be seen that the quantum emitters produced by both Ta and Ge ions irradiation maintain stable luminescence with almost no blinking and bleaching. However, we also found out that heavy ion irradiation could produce some unstable quantum emitters with photoblinking (the unstable PL spectrum of the quantum emitter in Supporting Information, S3), which is similar to the phenomenon reported in other literature.[25,30] The unstable luminescence should be attributed to the existence of nonluminescent point defects around the quantum emitters due to the randomness of heavy ions irradiation. As reported in literature,[40] there are multiple defects are localized with a point defect. These nonluminescent point defects can quench and scatter the nonequilibrium carriers around quantum emitters and finally lead to luminous blinking and bleaching.

Figure 6e,f shows the fluorescence saturation behaviors of quantum emitters by measuring the PL intensity as the function of excitation power. The red lines are the fitting curves according to the formula[49]

$$I = \frac{I_{sat}P}{P + P_{sat}} + bP + c \tag{1}$$

here, I_{sat} and P_{sat} are the saturation fluorescence intensity and saturation powers of the emitters, whereas b describes a potential contribution due to linear background emission stemming from the host material, and c is a constant, and its value is the fluorescence intensity at 0 W.

For Ta ion irradiation, the fluorescence emission intensity increases with the incident laser power, and basically, no saturation is visible when the incident power is as high as 67 mW. However, the quantum emitter generated by Ge ions reaches its maximum saturation brightness of 4.3×10^5 counts/s at about incident power of 3.5 mW. The different fluorescence saturation behaviors may be mainly attributed to the existence of nonluminescent point defects around the quantum emitter produced by Ta ions.

Figure 6g,h is the typical emission polarization of quantum emitters generated by Ge and Ta ions, suggesting that the quantum emitter also emits linearly polarized light. As reported in other literature,[9,23,49−51] the polarization data are fitted with the following formula:

$$I = I_0 \cos^2(\theta + \theta_c) \tag{2}$$

where I_0 is the maximum intensity and θ_c is the angle between the initial polarization direction of light and the transmission axis of the polarizer. The experimental results are in good agreement with the fitted red curves.

The degree of polarization (DOP) of emission light is calculated by the following formula:

$$\mathrm{DOP} = \frac{I_{max} - I_{min}}{I_{max} + I_{min}} \tag{3}$$

Here, the I_{max} and I_{min} are the maximum fluorescence intensity and the minimum fluorescence intensity, respectively. The polarization degrees of quantum emitters produced by Ta and Ge ions are 0.96 and 0.97, respectively, which are slightly better than the values reported in other literature.[49,52] The high degree of polarization is extremely good for the application of quantum emitters in quantum communications.

The photon wavelength of the quantum emitter is another critical parameter for actual applications. The static statistical distribution of PL peak wavelengths of the quantum emitters in the hBN samples after Ta and Ge ions irradiation is shown in

https://doi.org/10.1021/acsphotonics.1c00364
ACS Photonics 2021, 8, 2912−2922

Figure 7. Figure 7a–d is the static statistical distributions of peak wavelengths under Ta ion irradiation with three different fluences and the total distribution, respectively. Figure 7e–h is the static statistical distributions of peak wavelengths under Ge ion irradiation with three different fluences and the total distribution, respectively. For Ta ion irradiation, it is clear to see that most of the peak wavelengths are distributed in the range of 540–560 nm, and only a few emission wavelengths are around 600 and 520 nm. However, for Ge ion irradiation, the wavelengths straggling distribution in a large range of 560–640 nm with a central wavelength around 600 nm. Based on our data, it can be concluded that different irradiations lead to different photon wavelengths of quantum emitters, and Ta ion irradiation, rather than the Ge ion, is more suitable for the production of high purity quantum emitters.

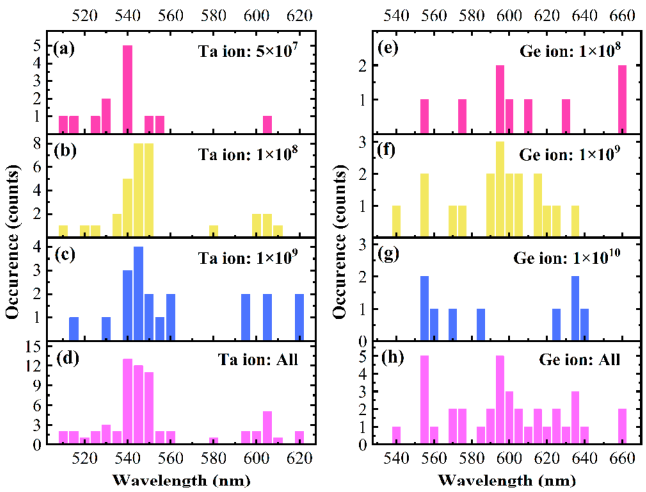

Figure 7. Statistic of the peak wavelength of quantum emitters in 2D hBN irradiated by Ta and Ge ions under different fluences. (a), (b), and (c) are the static statistics of the peak wavelength of the quantum emitters produced by Ta ions at fluences of 5×10^7, 1×10^8, and 1×10^9 ions/cm^2. (d) Static statistics of the peak wavelength of all quantum emitters produced by Ta ions. (e), (f), and (g) are the static statistics of the peak wavelength of the quantum emitters produced by Ge ions at fluences of 1×10^8, 1×10^9, and 1×10^{10} ions/cm^2. (h) Static statistics of the peak wavelength of all quantum emitters produced by Ge ions.

At present, defects that could act as quantum emitters in 2D hBN have been reported by literature through the first principles.[14,26,31,32,53,54] However, as different calculation methods were employed in the literature, their calculation results are quite different. Tran et al.[14] used the generalized gradient approximation of Perdew–Burke–Ernzerhof (PBE) to study the microphysical origin of the quantum emitters. However, due to the limitation of the PBE method itself, the calculated bandgap of hBN material was relatively small compared to the experimental value,[26,54] which made it impossible to accurately determine the origin of the quantum emitter. To obtain higher calculation accuracy, the spin-polarized hybrid density functional method (HSE06) was employed by Weston et al.[55] However, the structure they used was a few layers or a single layer of hBN.[14,26,53–55] Due to the thickness of the hBN flakes in our experiment is above a few nanometers, which is not consistent with the few-layer hBN structure, but is consistent with the bulk hBN structure. To get a more accurate result of the origin of the quantum emitters generated by heavy ions in hBN, we constructed the bulk structure of hBN and employed the HSE06 calculation method for first-principles calculations, which made our calculation results more consistent with the experimental results. Highly previous calculations of various defects in hBN were performed by Vienna Ab Initio Simulation Package in this work.[22,56] In the calculations, projector augmented wave (PAW) pseudo-potentials were used to describe the electron–ion interactions.[39,57] And generalized gradient approximation was employed as the exchange-correlation potential with the PBE parametrization method.[58,59] HSE06 were used to get the accurate description of the electronic structures,[32,60–62] and the mixing parameter in HSE06 was set to 31%. The plane-

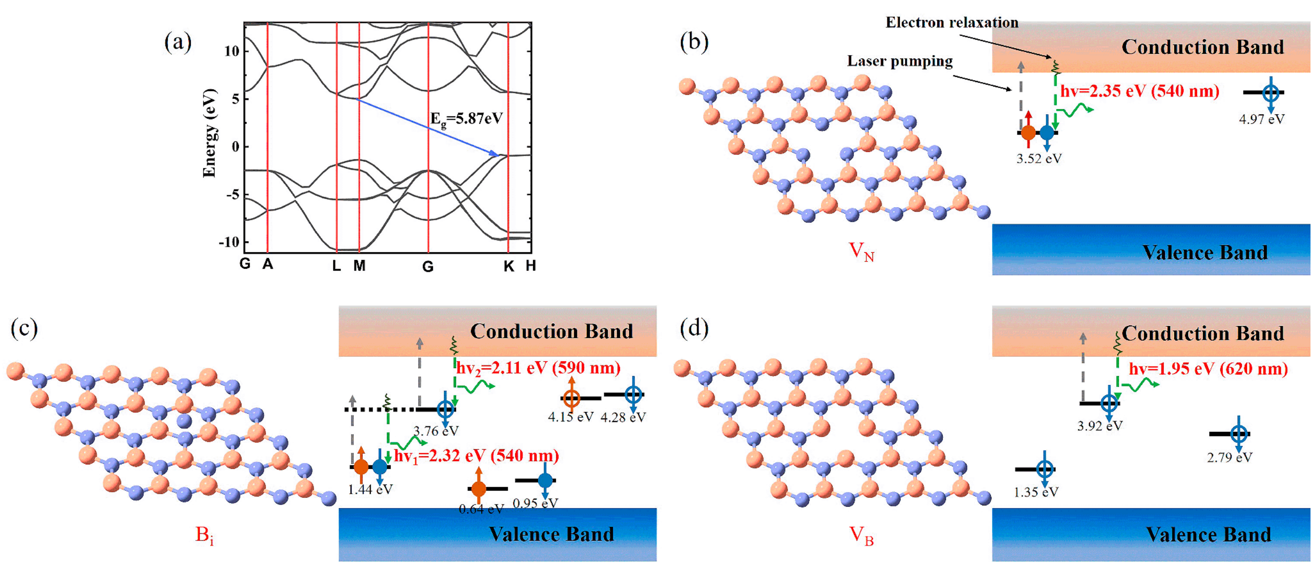

Figure 8. (a) Simulated band structure of bulk hBN with HSE06 hybrid functional method. Structure of point defects in hBN samples and corresponding band diagrams with defect energy levels: (b) V_N, (c) B_i, and (d) V_B. Black lines in the band gap represent the positions of the defect energy levels referenced to the valence band maximum. Red up arrows and blue down arrows denote the spin up and spin down directions, respectively. Red solid circles and blue hollow circles represent occupied and upoccupied defect energy levels by electrons, respectively.

https://doi.org/10.1021/acsphotonics.1c00364
ACS Photonics 2021, 8, 2912–2922

wave cutoff of 550 eV was used for all calculations. All the geometries were optimized until the Hellman−Feymann Force was less than 0.02 eV/Å.

As the 2D hBN flakes were mechanically exfoliated from high-quality bulk hBN, there were almost no impurities in them. Additionally, with high energies of heavy ions, nearly all of them passed through the flakes during the irradiation process, and a doping effect did not happen in the flakes. According to the GENAT4 simulation, the defects caused by the collision of heavy ions and hBN are all based on the intrinsic defects of B and N atoms (see Supporting Information, S4). Therefore, this calculation only considers the intrinsic point defects in hBN. According to current literature reports,[14,26,53,63] these intrinsic point defects in hBN that may become quantum emitters are selected, and first-principles calculations are performed on them. Here, six kinds of point defects and complex defects were considered. The point defects were nitrogen-vacancy (V_N), boron vacancy (V_B), boron antisite (B_N), nitrogen antisite (N_B), boron interstitial (B_i), and nitrogen interstitial (N_i), as shown in Figure 8b and Figure S3 in the Supporting Information. One of the complex defects was composed of a nitrogen antisite and a nitrogen vacancy nearest the nitrogen antisite, which was denoted as N_BV_N, as shown in Figure S3 in the Supporting Information (see Supporting Information, S5). Weston et al.[55] considered the different charge states of defects, and calculated the conversion energy levels. However, this method can only obtain the transition energy when the electron transitions between the band edge and the defect energy level, and cannot obtain the light emission when the electron transitions between the defect energy level.[55] Therefore, the luminous energy of defects cannot be fully understood. In addition, the physical origin of quantum emitters in hBN reported in the literature is almost always the neutral state of the defect,[14,26,53] which implies that the defects in the insulator-type hBN are more likely to be a neutral state. Therefore, we only considered the neutral state of the defect in the relevant calculations.

In the experiments, the thickness of the hBN flakes ranged from 4 to 30 nm, so they had a band structure similar to that of the bulk hBN. Therefore, a bulk hBN was used for the calculations in this paper. The calculated lattice parameters of bulk hBN were $a = b = 2.515$ Å, and $c = 6.690$ Å, which accord with the experimental values ($a = b = 2.50$ Å and $c = 6.66$ Å).[64] Band structure data calculated by the HSE06 method was dealt by a flexible toolkit of qvasp,[65] and a bandgap of 5.87 eV was obtained, which is in agreement with the experimental value of 5.89 eV,[66] as shown in Figure 8a. A 5 × 5 × 2 supercell with a number of 200 atoms was used to construct the defective structure. In the structure optimization, a Monkhorst−Pack scheme with a 2 × 2 × 2 k-point mesh was used, while a 1 × 1 × 1 k-point mesh was employed in the electronic structure calculations due to the large system of the supercell structure.

Band structures of V_N, B_i, and V_B are represented in Figure 8b−d. To find out the origin of the ZPLs of quantum emitters, three factors have to be considered when analyzing the band structures. The first one is that ZPLs can be generated by electron transitions between defect energy level and band edge and between defect energy levels.[14] The second factor is that when electrons jump between spin split energy levels, they must have the same spin direction. The last factor is that transition energy is not greater than 2.63 eV since the excitation wavelength is 473 nm with an energy of 2.63 eV.

Figure 8b−d shows the positions of defect energy levels in the band gap of the defective hBN structures, which are referenced to the valence band maximum. According to the above transition criteria, for V_N point defect shown in Figure 8b, electrons occupied on the defect energy level of 3.52 eV can be excited to the conduction band under laser illumination. After that, photons with an energy of 2.35 eV will be generated when these electrons transmit back from the conduction band, as displayed in the band diagram in Figure 8b. These photons are the origin of the peak around 540 nm of the PL spectra, as observed in Figure 7.

As for the defect of B_i shown in Figure 8c, electrons occupied on the defect energy level of 1.44 eV can be excited to the unoccupied defect level of 3.76 eV under laser illumination and then transmit back accompanied by release of photons with an energy of 2.32 eV. These photons are also responsibility for the peak around 540 nm of the PL spectra, as observed in Figure 7. In addition, it is possible for the electrons on the defect energy level of 3.76 eV to jump to the conduction band by absorbing laser light. Then these electrons will transmit back to the 3.76 eV defect level and release photons with an energy of 2.11 eV, which corresponds to the peak around 590 nm of the PL spectra, as observed in Figure 7.

As for the defect of V_B shown in Figure 8d, all the defect energy levels are empty. Electrons in the valence band can absorb laser light and jump to the conduction band through the defect energy levels of 1.35 and 3.92 eV, as illustrated in the band diagram in Figure 8d. When the electrons transmit from the conduction band to the defect level of 3.92 eV, photons with an energy of 1.95 eV will be released. These photons are the origin of the peak around 620 nm of the PL spectra, as observed in Figure 7.

According to the results based on the first-principles calculations, V_N and B_i point defects are responsible for the luminescence peak around 540−560 nm, and B_i and V_B point defects are the origin of the luminescence peak around 600 nm. For the other point defects and the complex defects mentioned above, electron transitions (see S5 in Supporting Information) between the defect energy level and band edge and between the defect energy levels do not match with the experimental results, so we do not show here. In summary, heavy ions irradiation produced V_N, V_B, and B_i point defects are quantum emitters in the hBN flakes.

In conclusion, high-energy Ta and Ge ions irradiations were used as an effective method to generate high-quality quantum emitters in the middle region of hBN flakes. Through the analysis of the production efficiency of quantum emitters, we found out that appropriate ion fluence and hBN thickness were critical parameters for quantum emitter generation due to atom displacement effect and layer interaction. The luminescence of quantum emitters is nonclassical light. Moreover, quantum emitters generated by heavy ions had good luminescence stability, polarization degree, and saturation intensity, which were extremely important for subsequent practical applications of quantum emitters. The wavelength distribution analysis pointed out that the Ta ion could create more purity quantum emitters than the Ge ion. Based on our experimental data and literature reports, we make a detailed comparison of the property of quantum emitters generated irradiated particles in hBN, such as Ta ions, Ge ions, Ga ions, neutron, and electron (see Supporting Information, S6). At last, the first-principles calculations were performed on the point defects in hBN, and the calculation results suggested that the V_N, V_B, and B_i point

https://doi.org/10.1021/acsphotonics.1c00364
ACS Photonics 2021, 8, 2912−2922

defects were in good agreement with the experimental results. Overall, as a feasible engineering method, Ta ion irradiation with a higher energy than the Ge ion, is better to create high-quality quantum emitters in 2D hBN flakes.

■ ASSOCIATED CONTENT

Supporting Information

The Supporting Information is available free of charge at https://pubs.acs.org/doi/10.1021/acsphotonics.1c00364.

> Section S1: The distribution of energy intervals between ZPL and PSB; Section S2: Raman characterization of hBN; Section S3: The time traces of the PL spectrum; Section S4: GENAT4 simulates heavy ion incidence hBN; Section S5: First-principles calculation; Section S6: Comparison of irradiated particles (PDF)

■ AUTHOR INFORMATION

Corresponding Authors

Bo Li – *The Key Laboratory of Science and Technology on Silicon Devices, Chinese Academy of Sciences, Beijing 100029, China*; Email: libo3@ime.ac.cn

Chengbing Qin – *State Key Laboratory of Quantum Optics and Quantum Optics Devices, Institute of Laser Spectroscopy and Collaborative Innovation Center of Extreme Optics, Shanxi University, Taiyuan, Shanxi Province 030006, China*; orcid.org/0000-0002-6822-5113; Email: chbqin@sxu.edu.cn

Zhengsheng Han – *The University of Chinese Academy of Sciences, Beijing 100029, China; The Key Laboratory of Science and Technology on Silicon Devices, Chinese Academy of Sciences, Beijing 100029, China*; Email: zshan@ime.ac.cn

Authors

Rui Gu – *The University of Chinese Academy of Sciences, Beijing 100029, China; The Key Laboratory of Science and Technology on Silicon Devices, Chinese Academy of Sciences, Beijing 100029, China;* orcid.org/0000-0001-5029-2716

Lei Wang – *The Key Laboratory of Science and Technology on Silicon Devices, Chinese Academy of Sciences, Beijing 100029, China*

Huiping Zhu – *The Key Laboratory of Science and Technology on Silicon Devices, Chinese Academy of Sciences, Beijing 100029, China*

Shuangping Han – *State Key Laboratory of Quantum Optics and Quantum Optics Devices, Institute of Laser Spectroscopy and Collaborative Innovation Center of Extreme Optics, Shanxi University, Taiyuan, Shanxi Province 030006, China*

Yurong Bai – *School of Nuclear Science and Technology, Xi'an JiaoTong University, Xi'an, Shaanxi Province 710049, China*

Xuewen Zhang – *The Key Laboratory of Science and Technology on Silicon Devices, Chinese Academy of Sciences, Beijing 100029, China*

Jie Liu – *The Institute of Modern Physics, Chinese Academy of Sciences, Lanzhou, Gansu Province 730000, China*

Gang Guo – *China Institute of Atomic Energy, Beijing 102413, China*

Xiaoting Shan – *The Key Laboratory of Science and Technology on Silicon Devices, Chinese Academy of Sciences, Beijing 100029, China*

Guodong Xiong – *The Key Laboratory of Science and Technology on Silicon Devices, Chinese Academy of Sciences, Beijing 100029, China*

Jiantou Gao – *The Key Laboratory of Science and Technology on Silicon Devices, Chinese Academy of Sciences, Beijing 100029, China*

Chaohui He – *School of Nuclear Science and Technology, Xi'an JiaoTong University, Xi'an, Shaanxi Province 710049, China*

Xinyu Liu – *The University of Chinese Academy of Sciences, Beijing 100029, China; The Key Laboratory of Science and Technology on Silicon Devices, Chinese Academy of Sciences, Beijing 100029, China;* orcid.org/0000-0003-0854-8559

Fazhan Zhao – *The Key Laboratory of Science and Technology on Silicon Devices, Chinese Academy of Sciences, Beijing 100029, China*

Complete contact information is available at: https://pubs.acs.org/10.1021/acsphotonics.1c00364

Notes

The authors declare no competing financial interest.

■ ACKNOWLEDGMENTS

This work was supported by the National Natural Science Foundation of China (Grants 61874135), the National Key Research and Development Program of China (2016YFB0901804), the Innovation Center of Radiation Application, China Institute of Atomic Energy (No. KFZC2018040203), and the Key Research Program of Frontier Sciences, Chinese Academy of Sciences (No. ZDBS-LY-JSC015). The work was carried out at the National Supercomputer Center in Tianjin, and the calculations were performed on TianHe-1(A).

■ REFERENCES

(1) Awschalom, D. D.; Bassett, L. C.; Dzurak, A. S.; Hu, E. L.; Petta, J. R. Quantum Spintronics: Engineering and Manipulating Atom-Like Spins in Semiconductors. *Science* **2013**, *339* (6124), 1174–1179.

(2) O'Brien, J. L.; Furusawa, A.; Vuckovic, J. Photonic quantum technologies. *Nat. Photonics* **2009**, *3* (12), 687–695.

(3) Castelletto, S.; Johnson, B. C.; Ivády, V.; Stavrias, N.; Umeda, T.; Gali, A.; Ohshima, T. A silicon carbide room-temperature single-photon source. *Nat. Mater.* **2014**, *13* (2), 151–156.

(4) Berhane, A. M.; Jeong, K. Y.; Bodrog, Z.; Fiedler, S.; Schroder, T.; Trivino, N. V.; Palacios, T.; Gali, A.; Toth, M.; Englund, D.; Aharonovich, I. Bright Room-Temperature Single-Photon Emission from Defects in Gallium Nitride. *Adv. Mater.* **2017**, *29* (12), 1605092.

(5) Tchernij, S. D.; Herzig, T.; Forneris, J.; Kuepper, J.; Pezzagna, S.; Traina, P.; Moreva, E.; Degiovanni, I. P.; Brida, G.; Skukan, N.; Genovese, M.; Jaksic, M.; Meijer, J.; Olivero, P. Single-Photon-Emitting Optical Centers in Diamond Fabricated upon Sn Implantation. *ACS Photonics* **2017**, *4* (10), 2580–2586.

(6) Iwasaki, T.; Miyamoto, Y.; Taniguchi, T.; Siyushev, P.; Metsch, M. H.; Jelezko, F.; Hatano, M. Tin-Vacancy Quantum Emitters in Diamond. *Phys. Rev. Lett.* **2017**, *119* (25), 253601.

(7) Nagy, R.; Widmann, M.; Niethammer, M.; Dasari, D. B. R.; Gerhardt, I.; Soykal, O. O.; Radulaski, M.; Ohshima, T.; Vuckovic, J.; Son, N. T.; Ivanov, I. G.; Economou, S. E.; Bonato, C.; Lee, S.-Y.; Wrachtrup, J. Quantum Properties of Dichroic Silicon Vacancies in Silicon Carbide. *Phys. Rev. Appl.* **2018**, *9* (3), 034022.

(8) Ma, X.; Hartmann, N. F.; Baldwin, J. K. S.; Doorn, S. K.; Htoon, H. Room-temperature single-photon generation from solitary dopants of carbon nanotubes. *Nat. Nanotechnol.* **2015**, *10* (8), 671–675.

(9) Choi, S.; Toan Trong, T.; Elbadawi, C.; Lobo, C.; Wang, X.; Juodkazis, S.; Seniutinas, G.; Toth, M.; Aharonovich, I. Engineering and Localization of Quantum Emitters in Large Hexagonal Boron Nitride Layers. *ACS Appl. Mater. Interfaces* **2016**, *8* (43), 29642–29648.

(10) He, Y.-M.; Clark, G.; Schaibley, J. R.; He, Y.; Chen, M.-C.; Wei, Y.-J.; Ding, X.; Zhang, Q.; Yao, W.; Xu, X.; Lu, C.-Y.; Pan, J.-W. Single Quantum Emitters in Monolayer Semiconductors. *Nat. Nanotechnol.* **2015**, *10* (6), 497−502.

(11) Chakraborty, C.; Kinnischtzke, L.; Goodfellow, K. M.; Beams, R.; Vamivakas, A. N. Voltage-controlled quantum light from an atomically thin semiconductor. *Nat. Nanotechnol.* **2015**, *10* (6), 507−511.

(12) Koperski, M.; Nogajewski, K.; Arora, A.; Cherkez, V.; Mallet, P.; Veuillen, J. Y.; Marcus, J.; Kossacki, P.; Potemski, M. Single photon emitters in exfoliated WSe2 structures. *Nat. Nanotechnol.* **2015**, *10* (6), 503−506.

(13) Srivastava, A.; Sidler, M.; Allain, A. V.; Lembke, D. S.; Kis, A.; Imamoglu, A. Optically active quantum dots in monolayer WSe_2. *Nat. Nanotechnol.* **2015**, *10* (6), 491−496.

(14) Tran, T. T.; Bray, K.; Ford, M. J.; Toth, M.; Aharonovich, I. Quantum Emission From Hexagonal Boron Nitride Monolayers. *Nat. Nanotechnol.* **2016**, *11* (1), 37−41.

(15) Cassabois, G.; Valvin, P.; Gil, B. Hexagonal boron nitride is an indirect bandgap semiconductor. *Nat. Photonics* **2016**, *10* (4), 262−266.

(16) Toth, M.; Aharonovich, I. Single Photon Sources in Atomically Thin Materials. *Annu. Rev. Phys. Chem.* **2019**, *70* (1), 123−142.

(17) Ding, X.; He, Y.; Duan, Z. C.; Gregersen, N.; Chen, M. C.; Unsleber, S.; Maier, S.; Schneider, C.; Kamp, M.; Hoefling, S.; Lu, C.-Y.; Pan, J.-W. On-Demand Single Photons with High Extraction Efficiency and Near-Unity Indistinguishability from a Resonantly Driven Quantum Dot in a Micropillar. *Phys. Rev. Lett.* **2016**, *116* (2), 020401.

(18) Bonaccorso, F.; Sun, Z.; Hasan, T.; Ferrari, A. C. Graphene photonics and optoelectronics. *Nat. Photonics* **2010**, *4* (9), 611−622.

(19) Grigorenko, A. N.; Polini, M.; Novoselov, K. S. Graphene plasmonics. *Nat. Photonics* **2012**, *6* (11), 749−758.

(20) Xia, F.; Wang, H.; Xiao, D.; Dubey, M.; Ramasubramaniam, A. Two-Dimensional Material Nanophotonics. *Nat. Photonics* **2014**, *8* (12), 899−907.

(21) Jiandong Qiao, J. Q.; Fuhong Mei, F. M.; Yu, Y. Single-photon emitters in van der Waals materials. *Chin. Opt. Lett.* **2019**, *17* (2), 020011.

(22) Chejanovsky, N.; Rezai, M.; Paolucci, F.; Kim, Y.; Rendler, T.; Rouabeh, W.; Favaro de Oliveira, F.; Herlinger, P.; Denisenko, A.; Yang, S.; Gerhardt, I.; Finkler, A.; Smet, J. H.; Wrachtrup, J. Structural attributes and photo-dynamics of visible spectrum quantum emitters in hexagonal boron nitride. *Nano Lett.* **2016**, *16* (11), 7037−7045.

(23) Xu, Z.-Q.; Elbadawi, C.; Toan Trong, T.; Kianinia, M.; Li, X.; Liu, D.; Hoffman, T. B.; Nguyen, M.; Kim, S.; Edgar, J. H.; Wu, X.; Song, L.; Ali, S.; Ford, M.; Toth, M.; Aharonovich, I. Single photon emission from plasma treated 2D hexagonal boron nitride. *Nanoscale* **2018**, *10* (17), 7957−7965.

(24) Ziegler, J.; Klaiss, R.; Blaikie, A.; Miller, D. J.; Horowitz, V.; Aleman, B. J. Deterministic quantum emitter formation in hexagonal boron nitride via controlled edge creation. *Nano Lett.* **2019**, *19* (3), 2121−2127.

(25) Ngoc My Duong, H.; Nguyen, M. A. P.; Kianinia, M.; Ohshima, T.; Abe, H.; Watanabe, K.; Taniguchi, T.; Edgar, J. H.; Aharonovich, I.; Toth, M. Effects of High-Energy Electron Irradiation on Quantum Emitters in Hexagonal Boron Nitride. *ACS Appl. Mater. Interfaces* **2018**, *10* (29), 24886−24891.

(26) Zhang, H.; Lan, M.; Tang, G.; Chen, F.; Shu, Z.; Chen, F.; Li, M. Discrete color centers in two-dimensional hexagonal boron nitride induced by fast neutron irradiation. *J. Mater. Chem. C* **2019**, *7* (39), 12211−12216.

(27) Eapen, J.; Krishna, R.; Burchell, T. D.; Murty, K. L. Early Damage Mechanisms in Nuclear Grade Graphite under Irradiation. *Mater. Res. Lett.* **2014**, *2* (1), 43−50.

(28) Walker, R. C.; Shi, T.; Silva, E. C.; Jovanovic, I.; Robinson, J. A. Radiation effects on two-dimensional materials. *Phys. Status Solidi A* **2016**, *213* (12), 3065−3077.

(29) Wang, T.; Yang, W.; Li, B.; Bian, R.; Jia, X.; Yu, H.; Wang, L.; Li, Xi.; Xie, F.; Zhu, H.; Yang, J.; Gao, Y.; Zhou, Q.; He, C.; Liu, X.; Ye, Y. Radiation-Resistant CsPbBr3 Nanoplate-Based Lasers. *ACS Applied Nano Materials* **2020**, *3* (12), 12017−12024.

(30) Proscia, N. V.; Shotan, Z.; Jayakumar, H.; Reddy, P.; Cohen, C.; Dollar, M.; Alkauskas, A.; Doherty, M.; Meriles, C. A.; Menon, V. M. Near-deterministic activation of room-temperature quantum emitters in hexagonal boron nitride. *Optica* **2018**, *5* (9), 1128−1134.

(31) Tran, T. T.; Zachreson, C.; Berhane, A. M.; Bray, K.; Sandstrom, R. G.; Li, L. H.; Taniguchi, T.; Watanabe, K.; Aharonovich, I.; Toth, M. Quantum Emission from Defects in Single-Crystalline Hexagonal Boron Nitride. *Phys. Rev. Appl.* **2016**, *5* (3), 034005.

(32) Jayakumar, H.; Shotan, Z.; Considine, C.; Mazkoit, M.; Fedder, H.; Wrachtrup, J.; Alkauskas, A.; Doherty, M.; Menon, V.; Meriles, C. Optical spectroscopy and photo modification of individual single-photon emitters in hexagonal boron nitride. *APS March Meeting Abstracts* **2017**, *2017*, F30−006.

(33) Tran, T. T.; Kianinia, M.; Nguyen, M.; Kim, S.; Xu, Z. Q.; Kubanek, A.; Toth, M.; Aharonovich, I. Resonant Excitation of Quantum Emitters in Hexagonal Boron Nitride. *ACS Photonics* **2018**, *5* (2), 295−300.

(34) Vogl, T.; Campbell, G.; Buchler, B. C.; Lu, Y.; Lam, P. K. Fabrication and Deterministic Transfer of High-Quality Quantum Emitters in Hexagonal Boron Nitride. *ACS Photonics* **2018**, *5* (6), 2305−2312.

(35) Geick, R.; Perry, C. H.; Rupprecht, G. Normal Modes in Hexagonal Boron Nitride. *Phys. Rev.* **1966**, *146* (2), 543−547.

(36) Reich, S.; Ferrari, A. C.; Arenal, R.; Loiseau, A.; Bello, I.; Robertson, J. Resonant Raman scattering in cubic and hexagonal boron nitride. *Phys. Rev. B: Condens. Matter Mater. Phys.* **2005**, *71* (20), 205201.

(37) Nemanich, R. J.; Solin, S. A.; Martin, R. M. Light scattering study of boron nitride microcrystals. *Phys. Rev. B: Condens. Matter Mater. Phys.* **1981**, *23* (12), 6348−6356.

(38) Bommer, A.; Becher, C. New insights into nonclassical light emission from defects in multi-layer hexagonal boron nitride. *Nanophotonics* **2019**, *8* (11), 2041−2048.

(39) Vuong, T. Q. P.; Cassabois, G.; Valvin, P.; Ouerghi, A.; Chassagneux, Y.; Voisin, C.; Gil, B. Phonon-Photon Mapping in a Color Center in Hexagonal Boron Nitride. *Phys. Rev. Lett.* **2016**, *117* (9), 097402.

(40) Hayee, F.; Yu, L.; Zhang, J. L.; Ciccarino, C. J.; Nguyen, M.; Marshall, A. F.; Aharonovich, I.; Vučković, J.; Narang, P.; Heinz, T. F.; Dionne, J. A. Revealing multiple classes of stable quantum emitters in hexagonal boron nitride with correlated optical and electron microscopy. *Nat. Mater.* **2020**, *19* (5), 534−539.

(41) Sajid, A.; Ford, M. J.; Reimers, J. R. Single-photon emitters in hexagonal boron nitride: a review of progress. *Rep. Prog. Phys.* **2020**, *83* (4), 044501.

(42) Mathew, S.; Chan, T. K.; Zhan, D.; Gopinadhan, K.; Barman, A. R.; Breese, M. B. H.; Dhar, S.; Shen, Z. X.; Venkatesan, T.; Thong, J. T. L. The effect of layer number and substrate on the stability of graphene under MeV proton beam irradiation. *Carbon* **2011**, *49* (5), 1720−1726.

(43) Nanda, G.; Goswami, S.; Watanabe, K.; Taniguchi, T.; Alkemade, P. F. A. Defect Control and n-Doping of Encapsulated Graphene by Helium-Ion-Beam Irradiation. *Nano Lett.* **2015**, *15* (6), 4006−4012.

(44) Borowicz, P.; Taube, A.; Rzodkiewicz, W.; Latek, M.; Gieraltowska, S. Raman Spectra of High-κ Dielectric Layers Investigated with Micro-Raman Spectroscopy Comparison with Silicon Dioxide. *Sci. World J.* **2013**, *2013*, 1.

(45) Hou, S.; Birowosuto, M. D.; Umar, S.; Anicet, M. A.; Tay, R. Y.; Coquet, P.; Tay, B. K.; Wang, H.; Teo, E. H. T. Localized Emission from Laser-Irradiated Defects in Two-Dimensional Hexagonal Boron Nitride. *2D Mater.* **2018**, *5* (1), 015010.

(46) Grosso, G.; Moon, H.; Lienhard, B.; Ali, S.; Efetov, D. K.; Furchi, M. M.; Jarillo-Herrero, P.; Ford, M. J.; Aharonovich, I.;

Englund, D. Tunable and high-purity room temperature single-photon emission from atomic defects in hexagonal boron nitride. *Nat. Commun.* **2017**, *8* (1), 1−8.
(47) Zhang, R.; Li, B.; Yang, J. Effects of stacking order, layer number and external electric field on electronic structures of few-layer C2N-h2D. *Nanoscale* **2015**, *7* (33), 14062−14070.
(48) Bjorkman, T.; Gulans, A.; Krasheninnikov, A. V.; Nieminen, R. M. van der Waals Bonding in Layered Compounds from Advanced Density-Functional First-Principles Calculations. *Phys. Rev. Lett.* **2012**, *108* (23), 235502.
(49) Lazic, S.; Espinha, A.; Yanguas, S. P.; Gibaja, C.; Zamora, F.; Ares, P.; Chhowalla, M.; Paz, W. S.; Palacios Burgos, J. J.; Hernandez-Minguez, A.; Santos, P. V.; van der Meulen, H. P. Dynamically tuned non-classical light emission from atomic defects in hexagonal boron nitride. *Communications Physics* **2019**, *2* (1), 1−8.
(50) Froch, J. E.; Kim, S.; Mendelson, N.; Kianinia, M.; Toth, M.; Aharonovich, I. Coupling Hexagonal Boron Nitride Quantum Emitters to Photonic Crystal Cavities. *ACS Nano* **2020**, *14* (6), 7085−7091.
(51) Vogl, T.; Lecamwasam, R.; Buchler, B. C.; Lu, Y.; Lam, P. K. Compact Cavity-Enhanced Single-Photon Generation with Hexagonal Boron Nitride. *ACS Photonics* **2019**, *6* (8), 1955−1962.
(52) Blascetta, N. P.; Liebel, M.; Lu, X.; Taniguchi, T.; Watanabe, K.; Efetov, D. K.; van Hulst, N. F. Nanoscale Imaging and Control of Hexagonal Boron Nitride Single Photon Emitters by a Resonant Nanoantenna. *Nano Lett.* **2020**, *20* (3), 1992−1999.
(53) Tawfik, S. A.; Ali, S.; Fronzi, M.; Kianinia, M.; Toan Trong, T.; Stampfl, C.; Aharonovich, I.; Toth, M.; Ford, M. J. First-principles investigation of quantum emission from hBN defects. *Nanoscale* **2017**, *9* (36), 13575−13582.
(54) Reimers, J. R.; Sajid, A.; Kobayashi, R.; Ford, M. J. Understanding and Calibrating Density-Functional-Theory Calculations Describing the Energy and Spectroscopy of Defect Sites in Hexagonal Boron Nitride. *J. Chem. Theory Comput.* **2018**, *14* (3), 1602−1613.
(55) Weston, L.; Wickramaratne, D.; Mackoit, M.; Alkauskas, A.; Van de Walle, C. G. Native point defects and impurities in hexagonal boron nitride. *Phys. Rev. B: Condens. Matter Mater. Phys.* **2018**, *97* (21), 214104.
(56) Zhu, H.; Zhang, G.; Wu, X. Injection of spin polarization into Si from the heterostructure $LaMnO_3$/Si interface. *Appl. Phys. Express* **2014**, *7* (9), 093003.
(57) Zhu, H.; Gu, M.; Huang, L.; Wang, J.; Wu, X. Structural and electronic properties of CdTe:Cl from first-principles. *Mater. Chem. Phys.* **2014**, *143* (2), 637−641.
(58) Zhu, H. P.; Zheng, Z. S.; Li, B.; Li, B. H.; Zhang, G. P.; Li, D. L.; Gao, J. T.; Yang, L.; Cui, Y.; Liang, C. P.; Luo, J. J.; Han, Z. S. Total dose effect of Al_2O_3-based metal-oxide-semiconductor structures and its mechanism under gamma-ray irradiation. *Semicond. Sci. Technol.* **2018**, *33* (11), 115010.
(59) Jaffrennou, P.; Barjon, J.; Lauret, J. S.; Attal-Tretout, B.; Ducastelle, F.; Loiseau, A. Origin of the excitonic recombinations in hexagonal boron nitride by spatially resolved cathodoluminescence spectroscopy. *J. Appl. Phys.* **2007**, *102* (11), 116102.
(60) Museur, L.; Anglos, D.; Petitet, J.-P.; Michel, J.-P.; Kanaev, A. V. Photoluminescence of hexagonal boron nitride: Effect of surface oxidation under UV-laser irradiation. *J. Lumin.* **2007**, *127* (2), 595−600.
(61) Museur, L.; Kanaev, A. Photoluminescence properties of pyrolytic boron nitride. *J. Mater. Sci.* **2009**, *44* (10), 2560−2565.
(62) Wang, X.; Pakdel, A.; Zhi, C.; Watanabe, K.; Sekiguchi, T.; Golberg, D.; Bando, Y. High-yield boron nitride nanosheets from 'chemical blowing': towards practical applications in polymer composites. *J. Phys.: Condens. Matter* **2012**, *24* (31), 314205.
(63) Sajid, A.; Reimers, J. R.; Ford, M. J. Defect states in hexagonal boron nitride: Assignments of observed properties and prediction of properties relevant to quantum computation. *Phys. Rev. B: Condens. Matter Mater. Phys.* **2018**, *97* (6), 064101.
(64) Lynch, R. W.; Drickamer, H. G. Effect of high pressure on the lattice parameters of diamond, graphite, and hexagonal boron nitride. *J. Chem. Phys.* **1966**, *44* (1), 181−184.
(65) Yi, W.; Tang, G.; Chen, X.; Yang, B.; Liu, X. qvasp: A flexible toolkit for VASP users in materials simulations. *Comput. Phys. Commun.* **2020**, *257* (1), 107535.
(66) Solozhenko, V. L.; Lazarenko, A. G.; Petitet, J. P.; Kanaev, A. V. Bandgap energy of graphite-like hexagonal boron nitride. *J. Phys. Chem. Solids* **2001**, *62* (7), 1331−1334.

https://doi.org/10.1021/acsphotonics.1c00364
ACS Photonics 2021, 8, 2912−2922